


An Embedded Tactical Decision Aid Framework for Environmentally Adaptive Autonomous Underwater Vehicle Communication and Navigation

EeShan C. Bhatt , Bradli Howard, and Henrik Schmidt, *Member, IEEE*

Abstract—Motivated by a changing acoustic environment in the Arctic Beaufort Sea, in this article, we present a tactical decision aid framework for a human decision-maker collaborating with an autonomous underwater vehicle (AUV) to integrate the vertical sound-speed profile for underwater navigation and communication. In a predeployment phase, using modeled and real oceanographic data, we load basis function representations of the sound-speed perturbations onto one or more AUVs on deck, where a handful of weights can estimate a sound-speed profile. During deployment, these weights are updated on an AUV through a digital acoustic message to improve navigation and reciprocal communication throughout the duration of an under-ice mission. Field work applying this framework in the Beaufort Sea is presented, highlighting key decisions regarding predeployment oceanographic data assimilation, CTD cast collection, and *in situ* weight choice. Selected examples evaluate the framework's ability to adapt to a depth-limited CTD cast and the appearance of an anomalous microlens feature in the profile. We show that the framework effectively balances the need to adapt in a changing acoustic environment in real time while maintaining operator trust in an AUV's embedded intelligence.

Index Terms—Human-computer interaction, operational oceanography, under-ice robotics.

I. INTRODUCTION

AUTONOMOUS underwater vehicles (AUVs) are an increasingly popular platform to explore and sample the ocean, particularly for remote or dangerous environments. Lightweight, mobile, and inexpensive compared to manned- and ship-based systems, these vehicles are becoming more capable with smaller payload sensors, faster computing power, and smarter embedded intelligence [1], [2]. But a major hurdle in considering AUVs as reliable and standard tools for oceanographic research is navigation uncertainty. While land

and air-based robots utilize satellite-based global positioning system (GPS) to achieve stunning location accuracy and precision throughout the duration of their missions, AUVs cannot access GPS while underwater due to the rapid attenuation of electromagnetic waves [3]. A vehicle can stall on the surface to receive a GPS fix, but this foolproof method of repositioning is inaccessible in an ice-covered environment or other GPS-denied situations.

Much work has been done in underwater vehicle navigation, which relies on any combination of dead reckoning, hydrodynamic models, inertial navigation systems (INS), doppler velocity logs (DVL), GPS fixes, and/or acoustic baseline navigation systems [4]. In particular, the long baseline (LBL) navigation system is the most similar in scale and style to GPS, and most appropriate for mitigating drift in underwater vehicle localization without overburdening computation on the vehicle [5]. Multiple distributed transponders, in fixed positions on the order of hundreds of meters to several kilometers, listen for vehicle range requests. They can send a message back such that the AUV can self-localize via two-way travel time ranging and trilateration. The advent of the WHOI micromodem [6] and synchronized chip scale atomic clocks [7] enabled ranging via one-way travel time (OWTT) [8]–[11].

For both one-way and two-way travel time configurations, however, accuracy in the range estimate in an LBL paradigm is limited by the environmentally sensitive relationship between range, travel time, and the sound-speed profile. For mesoscale (tens to hundreds of kilometers) navigation or localization efforts, a deterministic [12] or through-the-sensor [13] value for sound speed is used. Some postprocessing methods account for the depth dependence [14], spatio-temporal variability in the sound-speed profile to minimize error [12], [15], or specific ray paths [15]. Short range (less than ten kilometer) navigation efforts, on the other hand, can accurately rely on a nominal sound speed value and achieve minimal navigation error [9], [10], [16]. But this assumption breaks down in complex propagation environments such as the multipath incurred by the Beaufort Lens [17].

The Beaufort Lens is as a warm water intrusion in an intensely stratified water mass, creating a local temperature (and sound speed) maximum around 50–60 m. From the surface down, there is less saline surface water via ice melt; warm, saline Pacific Summer Water (forming the lens); cold Pacific Winter Water; warm, saline Atlantic water; and then Arctic Deep

Manuscript received 7 June 2021; revised 10 December 2021; accepted 8 March 2022. Date of publication 15 June 2022; date of current version 13 October 2022. The work of EeShan C. Bhatt was supported by the National Defense, Science, and Engineering Graduate Fellowship. This work was supported in part by the Office of Naval Research 322-OA under ICEX20 Grant N00014-17-1-2474 and in part by Task Force Ocean under Grant N00014-19-1-2716. (Corresponding author: EeShan C. Bhatt.)

Associate Editor: J. Gomes.

The authors are with the Center for Ocean Engineering, Department of Mechanical Engineering, Massachusetts Institute of Technology, Cambridge, MA 02139 USA (e-mail: eeshan@mit.edu; bradli@mit.edu; henrik@mit.edu).

Digital Object Identifier 10.1109/JOE.2022.3159234

Water [18], [19]. This stratification creates a unique double ducted environment that has drastic consequences for acoustic communication, sensing, and navigation compared to historical conditions of a monotonically increasing sound speed [20]. The upper duct, at the surface, keeps transmission loss low but severely degenerates signal coherence due to a higher degree of surface interacting paths. The lower duct, approximately between 50 and 200 m in depth, effectively traps sound above 300 Hz and can propagate sound at near-basin scales [21]. Here, we distinguish the lens as an oceanographic feature—the local temperature/sound-speed maximum, its variability, and effect on surrounding water masses—and the ducts as acoustic features dependent on source depth and frequency.

While the duct has been exploited for long range transmissions [13], [22], short range transmissions are marred by an acoustic shadow zone. This shadow zone is a predominant feature from 2 to 6 km in range for source depths of 33–200 m [21], engulfing the operational ranges and depths for AUV deployments. Furthermore, the strength of the duct is highly variable and not captured by publicly available models like hybrid coordinate ocean model (HYCOM) [23], a sea-ice coupled, three-hour resolution, $1/12^\circ$ resolution model well used by the ocean acoustics and naval intelligence communities [24]. A custom high resolution and daily surface forced MITgcm [25] modeling effort was able to represent the warm water layer as a persistent, widespread, but discontinuous feature [26], [27]. Long-term mooring deployments in the Beaufort Sea have shown that the largest observed sound-speed variability is in between 50 and 100 m in depth, due to warmer and saltier (spicier) water [28].

This work is motivated by under-ice AUV operations with four GPS-aided micromodem buoys, during the Ice Exercise 2020 (ICEX20), in March, in the Beaufort Sea. Environmentally driven AUV behavior was central to mission success given the total under-ice environment (necessitating accurate return to home) and the Beaufort Lens (obfuscating short-range propagation). The spatio-temporal variability of the Beaufort Lens predicates a locally updatable sound-speed profile for the integrated communication and navigation network [29], [30] depth-dependent adaption [21] and real-time acoustic ranging [24], [31].

In this article, we introduce a decision-making framework to facilitate robust environmental awareness in the Beaufort Sea, where profiler data reveals a complex acoustic propagation environment due to variable warming in the upper 100 m. We use a basis function representation of the sound speed to estimate a local sound-speed profile observation and compress the message content to a handful of weights; we call this the Virtual Ocean (VO). We also design and evaluate tactical decision aids (TDAs) to convey the joint environmental realism and acoustic utility for the various combinations of weights, i.e., various VO estimates from the basis function representation. We then communicate these weights to the vehicle via acoustic message to update its internal sound-speed estimate, which informs the navigation and communication behaviors. This framework was successfully deployed during Ice Exercise 2020 (ICEX20) from

March 8–12, 2020, where multiple messages were sent from a topside transponder to submerged assets to synchronize updated sound-speed information.

The rest of this article is organized as follows. Section II covers background material and reviews relevant literature. Section III introduces a generalized procedure for modular and robust environmental autonomy, and Section IV details experimental conditions for ICEX20. Section V presents selected results to demonstrate how the framework created guided decision-making. Finally, Section VI concludes this article.

II. RELATED WORK

This section will cover the relevant literature in empirical orthogonal function (EOF) analysis, tactical decision aid (TDA) development, and vehicle deployments in the Arctic. In this work, we use EOF analysis to create a basis function representation of the sound speed, which serve as the feature space for TDAs to assess the environmental realism and acoustic utility for vehicle communication and navigation.

A. Empirical Orthogonal Function Analysis

EOF analysis seeks to reduce a large data set but capture its underlying, characteristic variability. It is often associated with principal component analysis (PCA), which finds the power behind each characteristic feature to estimate the initial data set, and singular value decomposition (SVD), which is the decomposition of any rectangular matrix [32]. As these eigenmethods are numerically driven, with no parametric distributions or underpinning physics, it is important to not ascribe scientifically meaning structures in the data without additional evidence, testing, or insight.

Consider a demeaned $n \times p$ data matrix X describing p measurements of the same variable at n times. In our case, each row of X contains an observed sound-speed profile assimilated to p different depths. An EOF analysis calculates the eigendecomposition of C_{xx} , the associated autocovariance of the demeaned data matrix, which is by definition square

$$C_{xx} = X^t X \quad (1)$$

$$C_{xx} = E \Lambda E^t. \quad (2)$$

This solves for E , a $p \times p$ orthonormal matrix, detailing column eigenvectors e_i (also known as modes or EOFs), and Λ , the diagonal matrix of eigenvalues. The sum of all eigenvalues, or the trace of Λ , is equal to the total auto-covariance of the data. Dividing each eigenvalue λ_i over the trace of Λ indicates how much variance is explained by the i th EOF.

Importantly, the EOFs are mutually uncorrelated in space. The time evolution of each EOF, also referred to as principal components or weights, β_i , are similarly mutually uncorrelated in time. The weights pertaining to any EOF are found by projecting X onto the EOF; the unit of the initial measurement is preserved in the weights, not the EOFs. For the first EOF

$$\beta_1 = X e_1. \quad (3)$$

Thus, the demeaned data matrix X can be represented exactly as a sum of p weighted EOFs

$$X = \sum_{i=1}^p \beta_i e_i \quad (4)$$

but can be estimated with a subset of the first j EOFs, where $j \ll p$.

It is computationally efficient to perform an EOF analysis through an SVD analysis. The former must compute the auto-covariance matrix; the latter solves for a reduced amount of eigenvectors and values, at most $j \leq \min_{n,p}$. An SVD analysis is factored as

$$X = USV^t \quad (5)$$

where U is a $n \times n$ orthogonal matrix, V is a $p \times p$ orthogonal matrix, and S is $n \times p$ diagonal matrix with j singular values. The column vectors of V are the EOFs; the column vectors of U are the normalized weights associated with each EOF. The eigenvectors and weights are linked by the singular values of S , which are the square root of the eigenvalues from C_{xx} .

Given a 2-D data set, where one represents the dimension in which we want to represent structure, and the other represents the dimension realizations of this structure have been sampled, eigenmethods generated a weighted feature space to explain the maximum amount of variance in the data. Their applications for sound-speed variability are diverse: creating a sound-speed “data bank” [33]; modeling sound speed and current fields for tomography [34]; merging multiple partial depth data time-series to better approximated the mixed layer compared to extrapolation [35]; classifying acoustically stable areas [36]; and reconstructing internal wave trains for acoustic study [37].

B. Tactical Decision Aids

TDA, while used in the US Navy as early as 1972 to support mine countermeasures [38], rose to the forefront after a cruiser misidentified a civilian plane as a hostile military aircraft [39]. Wagner [40] distills the essence of a TDA—to assist a decision-maker by “assimilation and convenient presentation of data” and “analysis of the tactical problem beyond what is feasible by humans in a timely fashion.” By 1989, four TDAs with predominantly environmental inputs and tactical outputs—Navy Search and Rescue (NAVSAR), Environmental Strike Planning Aid (ESPA), Tactical Environmental Ship Routing System (TESR), and Chaff Planning and Prediction System (CHAPPS)—were designed specifically to assist decision-makers in stressful and/or complex scenarios. TDA development for AUVs plays a natural analogue for submarine operations. More recent TDAs optimize for multivehicle path planning [41], prepare an acoustic battlefield [42], and implement fuzzy logic to digest qualitative and quantitative wave height descriptions [43].

The root idea of TDAs—communicating information across digital and human boundaries while leveraging computation of the former and the heuristic judgment of the latter—drives

advances in fields as far as interactive architectural design [44] and, closer to home, human–robot interaction [45]–[47]. Thus, TDAs serve as organic documentation between human and AI decision-makers. The TDAs we present here are framed as operational guidance that modify robot behavior; they build on previous successful elements like text- and graphic-based recommendations, user-entered bounds, cost functions, and dynamic programming.

C. Autonomous Vehicle Deployments in the Arctic

We refer the interested reader to [48] and [49] for a thorough historical review of vehicle operations in polar environments. Here, we focus on how comparable recent autonomous vehicle deployments in the Arctic have not needed to consider the sound-speed profile in real-time for successful navigation and recovery.

Most AUV deployments under-ice in the Arctic have observed the historical, upward refracting sound-speed profile, where the isovelocity assumption does not introduce large error for short-range operations. AUV deployments in the summer of 2007 near the Gakkel Ridge observed greatly varying open ice leads, which posed challenges for a vehicle to surface [50]. But because the LBL beacons sat 150 m above the seafloor, and the majority of the vehicle’s mission was below 2000 m, slant ranges were accurately calculated using a depth-averaged sound speed [51]. Cross-shore transects taken under coastal sea ice relied on an ultrashort baseline homing system to ensnare the AUV in a net [52], [53].

Other AUV missions have demonstrated success in partial or ice-free conditions with inherently higher tolerance for navigation error. Vehicles have been applied to map several important oceanographic processes including glacially modified waters [54], horizontal density structure [55], and surface fronts [56]. It was not until glider deployments in September 2014, in the northern Chukchi and Beaufort Seas, that a vehicle operated in the Beaufort Lens’ double ducted environment. The initial experiment exploited the lower duct for highly accurate long-range transmissions, but acoustic navigation was untenable outside of the duct [13], [22]. In September 2017, a follow-up glider deployment showed that glider renavigation using an acoustic arrival method and the average sound-speed profile from the gliders reduced positioning error by a factor between four and five depending on the dive [12].

III. GENERALIZED VIRTUAL OCEAN FRAMEWORK

This section will introduce a generalized framework for environmentally adaptive behavior in the VO paradigm. A schematic detailing the operational procedure into four steps is shown in Fig. 1.

A. Predeployment Phase

First, in the predeployment phase [see Fig. 1(a)], multiple sound-speed training sets are formed. Each training set can be populated by any set of relevant models and/or observations, assimilated to the same depth grid, and demeaned with

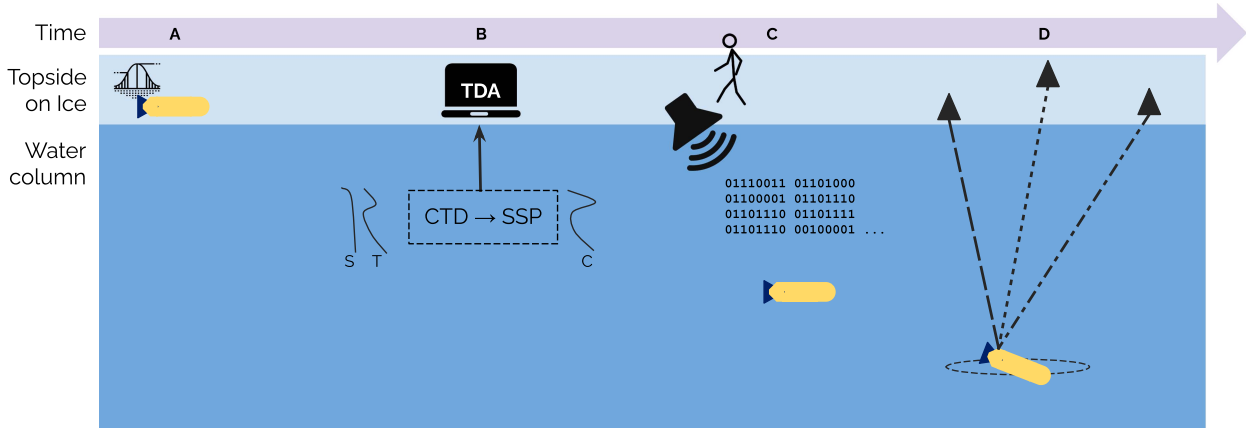


Fig. 1. Visual diagram of the Virtual Ocean approach. (a) Preload several basis function representations of the sound-speed environment for a space-time region of interest. (b) Acquire new SSP information. Through interactive graphical tools, isolate a basis function and evaluate weights based on environmental realism and acoustic utility. (c) Send the weights via lightweight acoustic message. (d) Updated SSP is used for environmentally adaptive communication and navigation behaviors. The overall framework enables the same updatable sound-speed estimate on topside and the AUV.

a depth-dependent sound-speed mean. The depth-dependent sound-speed mean is used, opposed to a scalar value, such that a series of null weights would be somewhat realistic. The EOF shapes are smoothed with a small spatial filter to encourage sound-speed continuity at the cost of perfect orthogonality. Custom VO files are created and preloaded onto the vehicle, where each one contains the depth-dependent sound-speed mean; an EOF basis set; a corresponding depth vector; and kernel density estimates (KDE) for the weights for every EOF from the training set. By the nature of EOF analysis, the resulting sound-speed estimates have no knowledge of bathymetry or bottom properties. A companion bathymetric file with 1-min resolution is supplied [57] and bottom properties are set manually.

B. Interactive Tactical Decision Aids

Next, just before vehicle deployment, an initial external conductivity, temperature, and depth (CTD) cast is taken to get a local observation of the sound-speed profile in the deployment area [see Fig. 1(b)]. Through the TDA framework, a decision-maker compares this real sound-speed profile to the training sets and chooses an initial VO file and weights to best estimate the desired sound speed while preserving historical variability. The basis set is confirmed for the mission duration, and the initial weights are sent to the vehicle via an acoustic message as it begins its mission. In the scenario where no EOF set accurately described the sound-speed profile, a backdoor was built in to modify the base sound-speed value directly. This would impose previously studied variability onto a new mean. The vehicle would begin its mission with all EOF weights set to zero; these weights could be updated accordingly throughout the mission, with reference to the initial anomalous CTD cast.

With this first ground truth CTD (or a subsequent one, if enough time has passed), a decision algorithm distills the environmental and acoustic realism for various EOF SSP estimates. The sound-speed estimates are least squares projections of the

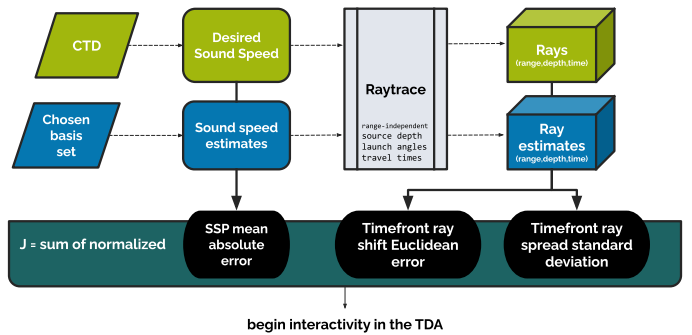


Fig. 2. Diagram of the decision algorithm to convey joint environmental and acoustic utility given a new sound-speed profile via CTD cast. The top layer, in green, shows the flow of real data; the middle layer, in blue, shows the flow of simulated data; the bottom layer, in teal, shows the cost function to compare the two. The parameters for the ray tracing are user configurable, but did not change from the defaults, which were informed by previous virtual experiments. The defaults were: source depth = 30 m, OWTT = 0.6, 1.3, 2, 3, 4, and 5 s; launch angles = $-30:5:-15^\circ$, $-10:2:10^\circ$, $15:5:30^\circ$, and a bottom depth of 2680 m.

observed sound-speed perturbation with respect to the EOF basis; the decision algorithm iterates through every possible combination of weights. Fig. 2 sketches out the TDA data and simulation pipeline.

The environmental realism is assessed by the mean absolute error between the desired sound-speed profile from the CTD c_z , and the estimate from the EOFs \hat{c}_z , in the interpolated depth grid from the EOFs to the maximum depth of the CTD. The environmental penalty ϵ_c is as follows:

$$\epsilon_c = \frac{\sum |\hat{c}_z - c_z|}{N_z}. \quad (6)$$

Acoustic penalties directly derive from timefronts along rays to align with timing and positioning mechanisms for navigation. The ray tracing solution implemented here is custom built [58] to be more computationally efficient than BELLHOP [59] for

this use case, as it does not produce any binary files and only reports the outputs necessary to drive the acoustic metrics. Because our operations are on small scales and the Arctic is a generally upward refracting environment, bottom interactions are simplified with a constant bathymetry. However, it would be trivial to include a 2-D bathymetry in a region where bottom effects were pronounced. Scattering from the ice surface is ignored to maintain interpretability of the acoustic penalties.

The raytracing function Γ , inputs c , a sound-speed profile; θ , a list of ray launch angles; t_{\max} , the maximum travel time desired; and z_{\max} , a nominal water column depth. It outputs ray positions in range and depth, P_{rz} , indexed by launch angle and list of travel times

$$P_{rz}(t, \theta) = \Gamma(c, \theta, t_{\max}, z_{\max}). \quad (7)$$

The raytracing function is run for both c_z and \hat{c}_z , with all other parameters defined the same. We define ray shift as the difference of the timefront locations of rays of the same launch angle between the desired and estimated sound speeds. The first acoustic penalty ϵ_{rz} looks at the magnitude of the error in Euclidean space. The second acoustic penalty ϵ_σ is simply the standard deviation of the ray shift, where $n_{\theta,t}$ is the total number of launch angles multiplied by the total number of interpolated travel times. Both preserve the units of distance in meters

$$\epsilon_{rz} = \|P_{rz} - \hat{P}_{rz}\| \quad (8)$$

$$\epsilon_\sigma = \sqrt{\frac{\sum |P_{rz} - \hat{P}_{rz}|}{n_{\theta,t}}}. \quad (9)$$

To normalize the differences in scale and units across all penalties, each is converted to a z-score, to minimize the overall cost function J

$$J = z(\epsilon_c) + z(\epsilon_{rz}) + z(\epsilon_\sigma). \quad (10)$$

The cost function returns an initial ranking of sound-speed estimates. The ranking is not a greedy estimator—more EOFs do not always perform better, as shown in Appendix A.

Sorting the cost function J produces an initial ranking of sound-speed estimates for the user. The top choice is automatically loaded into all the graphical interpretations distilling the environmental and acoustic penalties (discussed in Section V). The user can investigate any other ranking through a prompted entry, which updates the graphical components accordingly. Eventually, a ranking can be selected which preserves the simulation state, visual elements, and initializes (but does not send) the command to update weights on the submerged AUV. Thus, the responsibility for any tactical choice remains with the authoritative decision-maker.

C. Acoustic Message

While the VO file is chosen once per mission, weights can be resent at any time given another CTD cast, at the discretion of the topside decision-maker [see Fig. 1(c)]. These updates are marshaled via lightweight messages comprised of bounded basic

variable types, necessitated and designed for a low bandwidth acoustic channel [60], and are sent via a WHOI micromodem [6] with a 10-kHz carrier frequency, 5-kHz bandwidth, and phase-shift keying modulation; they were received on the AUV with the same micromodem.

D. Environmentally Adaptive Communication and Navigation Behaviors

The VO estimation interfaces directly into acoustic models to inform communication and navigation. The acoustic models [59] included 2-D bathymetry from the VO bathymetry file as well as a roughness parameter for ice scattering.

For navigation, the sound-speed information was used to estimate an effective horizontal group speed for each transmission path between an AUV and the four GPS-aided modem buoys [24], [31]. This ensured a reliable, physics-based method of converting OWTT to range that resulted in navigation accuracy on the order of meters.

For communication, the sound-speed information from the VO was used to seed depth adaptive behaviors. The vehicle inputted SSP, navigation message content (source depth, estimated position), and its self-position estimate into an onboard acoustic model to maintain optimal depth for communication [61]. Each LBL modem contained receive channels at 30 and 90 m in depth and a transmit channel at 30 or 90 m in depth. A synergistic self-adapting behavior determined what receive and transmit elements should be active [30].

IV. EXECUTION OF TDA FRAMEWORK DURING ICEx20

This section details the performance of the Virtual Ocean and interactive TDA framework for ICEx20. This begins with predeployment data assimilation to make an EOF basis, covers the CTD casts and the corresponding weights, and ends with a retrospective analysis on the environmental and acoustic penalties. The communication and navigation performance is beyond the scope of this article and has been initially covered by related work [24], [30], [31], [61].

In our field tests, the cost function J was solved for within two minutes, roughly scaling to a second per synthetic sound-speed estimate on a 8-core, 16-GiB RAM laptop. Additionally, colors and linestyles were chosen to be distinct for deuteranomaly, a visual disability that affects roughly 5% of men [62]; those colors are preserved here.

A. Data Assimilation and EOF=Analysis

To isolate different snapshots of sound-speed variability, six total tuned EOF sets were created using modeled and real data from March of 2013, 2019, and 2020. The latter two years, 2019 and 2020, were chosen for temporal proximity; 2013 was chosen for its similarity to trends in Northern Hemisphere sea ice extent provided by the National Snow and Ice Data Center [63] a few days before ICEx20. Fig. 3 details the spatial information for the modeled and real data inputs over the Beaufort Sea as well as the location for ice camps during 2016 and 2020, Camp Sargo and Seadragon, respectively.

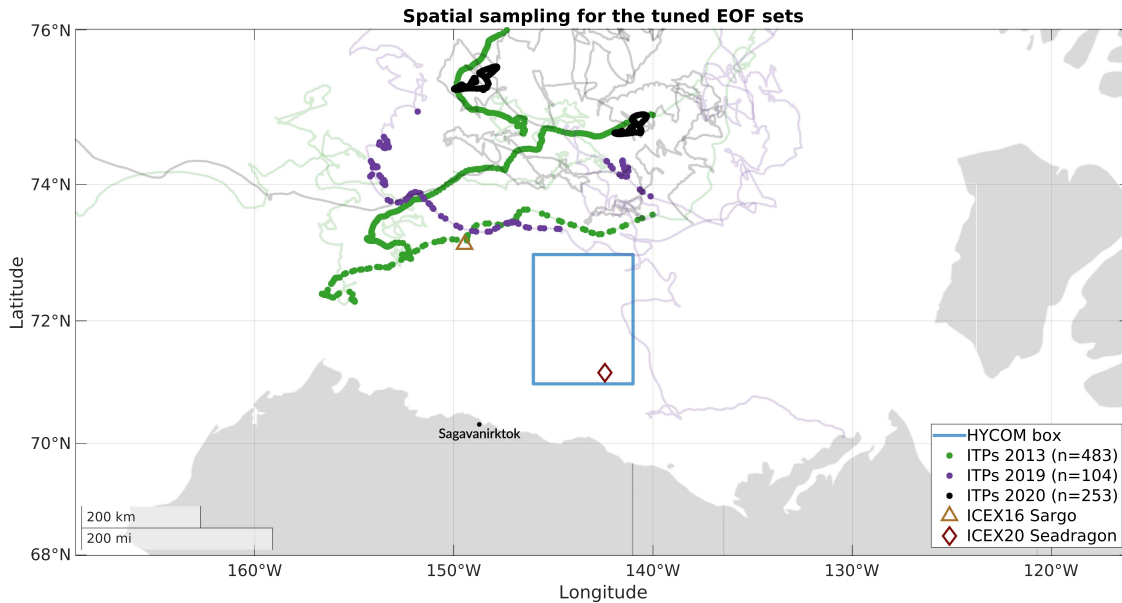


Fig. 3. Map of the spatial distribution for the tuned EOF sets. For ITP data, the lines indicate the path of various profilers whereas the dots indicate which profiles exist within the spatio-temporal region of interest. All spatial region of interests are the same, 70 to 76 N, 140 to 160 W. The temporal regions were manually adjusted to get enough data which would be supplemented by HYCOM k-means clustering, where $n:k = 4:1$. ITP 2013 samples from February 1, 2013 to April 30, 2013. ITP 2019 samples from January 1, 2019 to May 30, 2019. ITP 2020 samples from February 1, 2020 to March 4, 2020, the day all EOF sets were finalized before the team shipped off to ICES20.

Model outputs were provided by the Hybrid Coordinate Ocean Model (HYCOM) Global Ocean Forecast (GOFS) 3.1 [64]. The model output was downloaded from March 4–13 with a three hour time step, from 71 to 73 N and 141 to 146 W, a few days before ICES20. The exact location of Camp Seadragon was not known when downloading the HYCOM outputs, just that it was southwest of the ICES16 location. It is important to note that the HYCOM output for 2013 is “reanalysis” data, which assimilates the HYCOM “analysis” with observed temperature and salinity profiles. The HYCOM output for 2019 and 2020 is simply “analysis” data.

Data outputs were provided by the Woods Hole Oceanographic Institution’s Ice Tethered Profiler (ITP) program [65], [66]. Data from all ITP profilers were filtered within 70 to 76 N and 140 to 160 W, around March of each year. The profiles, with depth sampling every two meters, were assimilated to the 40-point standard depth grid from HYCOM to capture the overall impression, not the microstructure, of the sound-speed profile. Due to sea ice, profilers rarely reach the surface. Due to instrument operating depth, profilers do not exceed 800 m. Profiles with valid data above 20 m were linearly extrapolated to the surface. Profiles with valid data below 600 m were continued to the maximum depth of HYCOM (4000 m) with the hydrostatic sound-speed gradient of 0.0167 m/s/m. The HYCOM depth grid ensured that the number of unique profiles was much greater than the number of depth grid points ($n \gg p$). In hindsight, we recommend that n should be at least an order of magnitude greater than p .

Half of the sets were trained only on modeled data and the other half blended real data and k-means clusters from models in a 4:1 ratio. Modeled data were necessary in every training set to populate the full water column. Fig. 4 shows

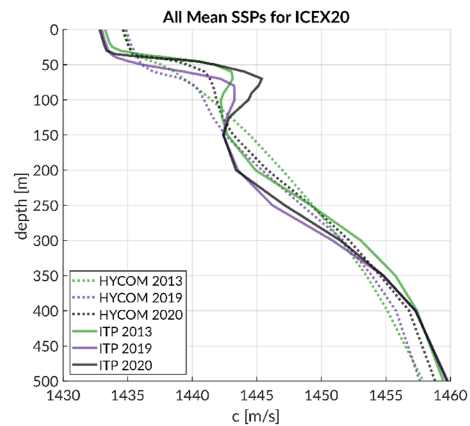


Fig. 4. Base values for sound speed across the training sets show a variety of duct strengths and heights. The “ITP” label indicates those that were trained on models and data; the “HYCOM” label indicates those that were trained on model output only.

the depth-dependent sound-speed mean for each training set; the ones trained with ITP data show a Beaufort Lens feature of varying strength, whereas the ones trained without data are reminiscent of the classical Arctic sound-speed profile.

Fig. 5 shows the first 7-EOF shapes with the cumulative variance explained and Fig. 6 shows the kernel density estimate for the ITP 2013 set. Together, these figures demonstrate that as the variance explained begins to plateau, the associated weight KDE begins to look more Gaussian and zero-centered. The VO files were truncated to 7 EOFs based on this insight, as higher order EOFs after this may be encoding more noise than signal.

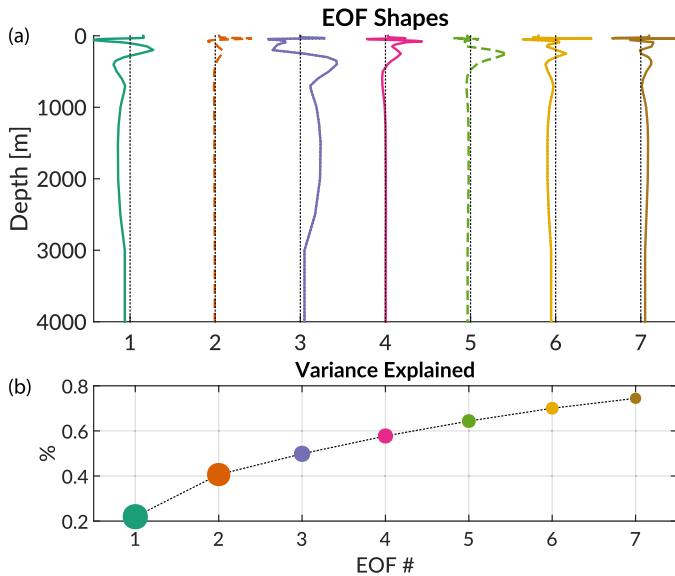


Fig. 5. (a) EOF shapes and (b) variance explained for the ITP 2013 training set. The EOF shapes themselves actually extend down to the maximum valid depth in HYCOM (4000 m), but most of the variance is in the upper 500 m. The shapes shown here are normalized such that the maximum values across all of them are the same.

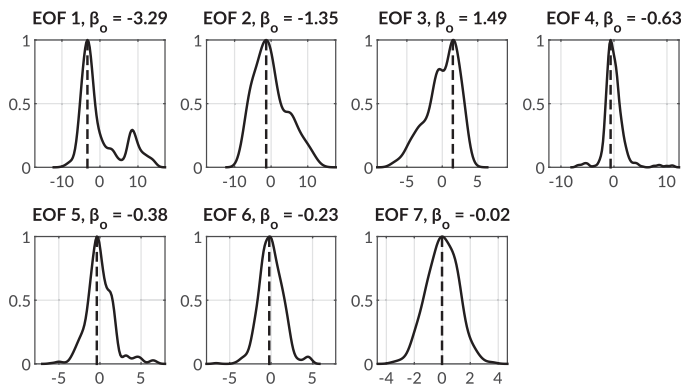


Fig. 6. KDEs for each EOF from the ITP 2013 database, nominally β , where β_o is the maximum likelihood from each distribution.

B. Choosing a Mission EOF Set

A single EOF set is chosen to parameterize the entire mission's Virtual Ocean based off a driving CTD (the second CTD in Fig. 7). We assume this CTD is representative enough of the ocean state for short, small-scale operations. The tuned EOF sets from ITP 2013 and HYCOM 2019 both estimated the driving CTD with less than $\epsilon_c \leq 0.5$ m/s. Ultimately the ITP 2013 set was chosen because it had better visual agreement and its baseline profile included a duct. Taking multiple CTD profiles in the week before deployment would have allowed this choice to be more quantitatively than qualitatively driven.

While we included the 2013 data based on first-order interactions between sea ice melt and growing heat content in the Pacific Summer Water [67], it is an oversimplification to claim that the sea ice extent explains the variability with the Beaufort Lens variability, especially since it is also the most populated data set. This EOF set was most valid for our

observed conditions; at another location and/or time, a different one may have performed best.

Interpreting the impact of the choices of initial databases on SSP estimation is not straightforward, especially with only four days of CTD data. The data-blended EOF sets tended to outperform the model-driven ones, likely because HYCOM has a high degree of redundancy and does not capture ducted conditions well.

Though the ITP 2013 EOF set was successful in SSP tracking over the course of ICEX20, it would not have been difficult to include an EOF set for March-like conditions of every year since 2010, or use statistical or machine learning methods to make EOF sets based on different degrees of ducting.

C. All ICEX20 CTDs

Ten CTDs were cast from an ice hole over the three-and-a-half-day experiment, roughly 250 km northeast of Sagavanirktok (Prudhoe Bay), Alaska. As shown in Fig. 7, the first five were from the RBR Concerto 3 (RBR), a retrievable plastic sensor that was operated on a manual winch down to a maximum of 400 m; the latter five were from the Lockheed Martin XCTD-1 (XCTD), which is expendable but goes to much greater depth. The accuracy of the XCTD is about an order of magnitude less than the RBR for temperature, conductivity, and pressure, but more than accurate to match the standard depth grid HYCOM provides. The top two meters from all CTD casts were discarded to eliminate observations that drifted warmer due to sensor stagnation in a heated ice hut.

Concurrent modeling or data assimilation set is a realistic benchmark for the EOF system. The HYCOM reanalysis was interpolated to the exact time, latitude, and longitude of the CTD casts. The reanalysis drastically mischaracterizes the sound-speed conditions as the classical Arctic conditions, as there is not a duct nor any significant changes in the sound-speed profile throughout the experiment.

The nearest ITP data, weighted by space and time, were retrieved shortly after ICEX20. These profiles capture a duct but the lens is 20–30 m deeper than those of the CTDs. There is better fit in the maximum sound speed of the observed duct, but naturally, due to the sparse nature of ITP observations, they are not sensitive to the local ICEX20 duct weakening, most evidenced from March 11 0630 onward.

The chosen EOF weights, drawn in a dotted black line, more accurately represent the local sound-speed conditions and produce reasonable estimates for sound speed beyond the CTD depth as well. The “dominant” sound-speed profile for ICEX20, observed in all RBR casts and the first XCTD cast, is extremely well fitted by the EOF set. There is some mismatch around 175 m, where the depth grid spacing loses resolution—from 100, 125, 150, and then 200 m.

From March 11 0630 onward, the duct develops a microlens that continues to shift in later observations. This feature is fairly unstable and not well characterized by the EOF set. Going through each of the four relevant CTDs, the chosen weights ignore the microlens; match the microlens by misfitting at 150 m; match a weaker duct because of no observed microlens; and ignore the microlens. Eventually, the tactical choice, enabled by

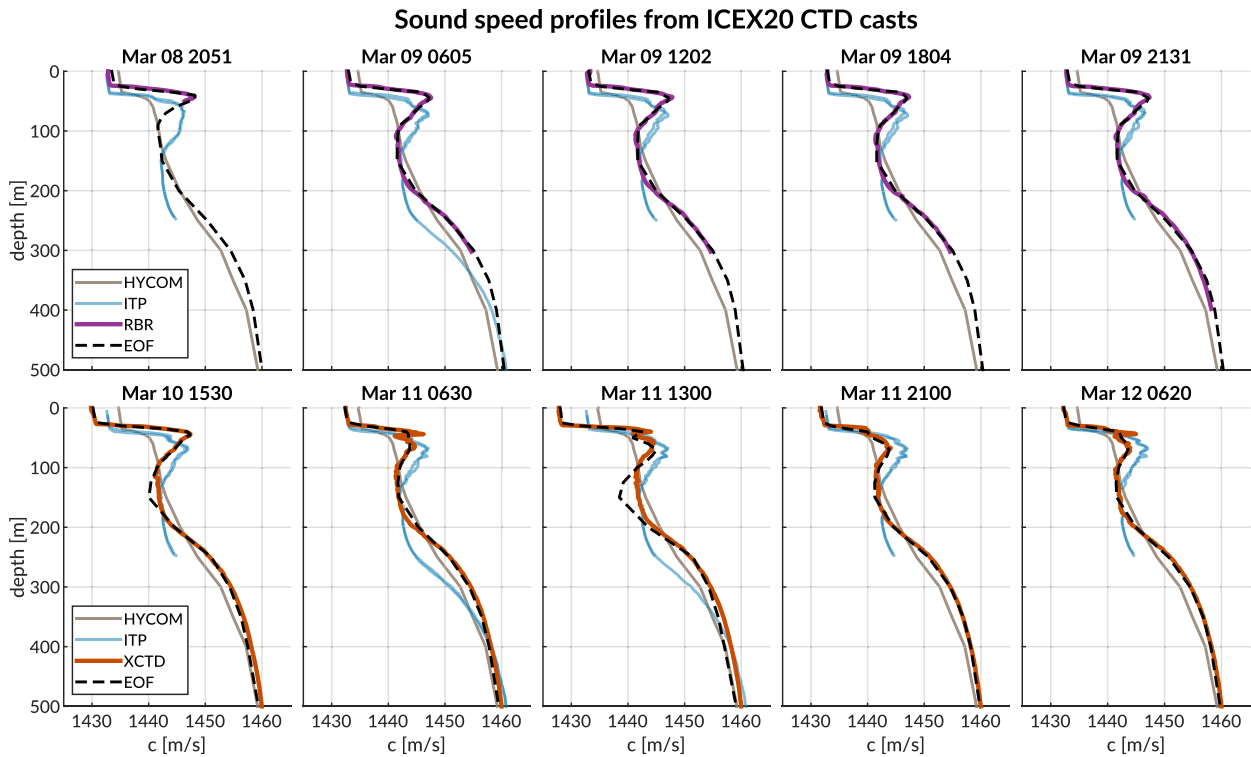


Fig. 7. All of the ICEX20 CTDs compared to other data streams with the chosen sound-speed estimates by decision-makers. For comparison, HYCOM is interpolated to the exact times, latitude (roughly 71.18° N), and longitude (roughly 142.41° W). The ITP data averages the nearest eight profilers in space and time. The initial plan was for a CTD cast every three hours to match HYCOM's temporal resolution; due to technical difficulties, we took ten over the course of three and a half days, with two different sensors. All times are Alaska time.

the TDA, was to ignore an unstable and acoustically minimal microlens. Overall, each sound speed is matched with a mean absolute error no greater than 1 m/s. The fluctuations across the ten CTDs provide strong narrative evidence that frequent CTD casts are necessary, even for short-term deployments, as the duct changes overnight between March 10th and 11th. The duct changing more likely represents the environment changing as a function of space and time than camp moving into new water given that the ice drift was unprecedentedly small, less than one cm/s. The final CTD was roughly only 2 km south of the first one.

D. Chosen Weights

Knowing that the sound-speed profile was overall well represented, we were interested to see how “predictable” these sound speeds could have been. A comparison of the discrete weights chosen for ICEX20 CTDs w compared to the distribution of weights from the training set β , as shown in Fig. 8, indicates that a bootstrapping technique would have likely captured the sound-speed profiles observed.

For all chosen weights, only β_6 and β_7 go beyond the *a priori* distribution when matching the microlens, further suggesting that it is an anomalous feature. The majority of chosen weights for all observations fall within the *a priori* distribution such that a probability distribution encoding may be of practical use [68]. The exceptions to this pattern, most evident in β_6 , may be easily remedied by extending the encoding domain.

When looking at the temporal spread of chosen weights, we see a consistency in the first five CTDs. The first CTD, which only went down to 50 m, is a narrow exception, as it only uses the first two weights. This was a tactical choice to not overfit the data provided. The sixth CTD, the first of the XCTDs, has slightly different weight mapping even though the sound-speed profile is similar; this is because the CTD cast itself is deeper, so the weighting is influenced by a different basis. Future work could add an element of interactivity to the TDA to modify the default uniform weighting of depth grid points. The chosen weights for the rest of the XCTDs are not as consistent, due to ill-fitting of the microens, but show the efficacy of a minimal message to update the internal sound-speed estimate on a submerged asset.

As expected, all of the chosen weights use w_1 . But the natural extension of that, that less dominant EOFs might be used less, is not strictly observed as β increases. For example, w_2 is skipped twice; w_3 is skipped thrice; w_4 is only skipped once. A simple rank sum for each CTD, across all the estimates that performed better than the mean ranking, finds that the second EOF was the most consistent driver behind the first eight CTDs; the sixth EOF governed the last two CTDs.

E. Correlation Between Acoustic and Environmental Penalties

Lastly, a comparison of environmental and acoustic penalties demonstrates the nonlinear relationship between the two, and by extension, the necessity for a TDA to convey a joint utility when

Chosen CTD weights projected onto the tuned distribution

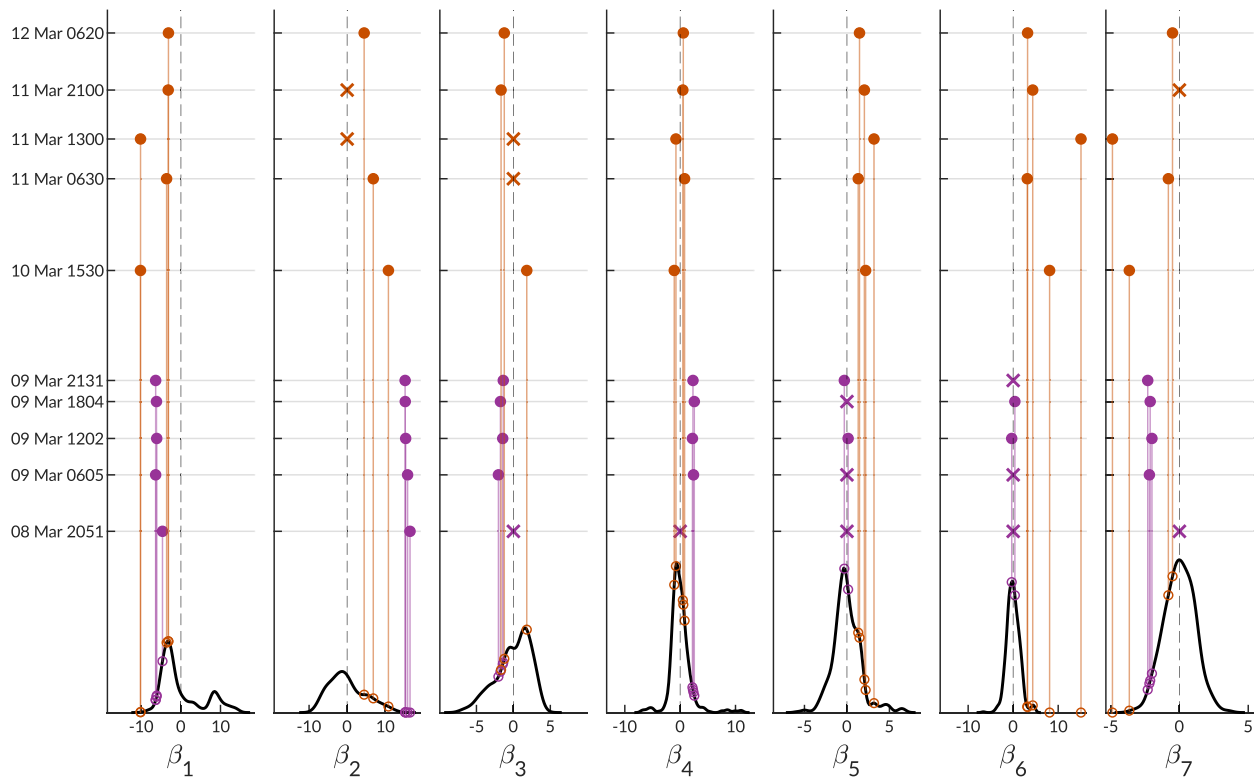


Fig. 8. Comparison of each CTD's chosen weights, w , to the training set distribution, β . The y-axis preserves the timestamp of each weight. The x-axis shows the kernel density estimate for the principal components provided by the EOF training set. Purple dots correspond to RBR and orange dots correspond to XCTD. Weights indicated by \bullet are nonzero (chosen) values, whereas an \times indicates a null value.

estimating the sound speed. Fig. 9 shows ϵ_c , the mean absolute error of the sound speed, on the x -axis, and ϵ_{rz} , the ray shift, on the y -axis.

The chosen weights for the first CTD, which has very little depth information, were initially ranked fiftieth. The ranking algorithm does not reward using fewer weights, but presents the information in an easy enough way to find them in the case of a lack of data or mistrust of sensor data. The other ranks chosen have a mode of 1 and a median of 5, so the ranking algorithm is aligning with decision-maker agreement. Rarely are the chosen ranks the minimal environmental and acoustic penalties. In addition to the mismatch between top ranks, there was a strong instinctual element in the decision-maker's process, i.e., simply not liking the shape of a particular sound-speed perturbation at a depth of interest, or a preference for acoustic parameters over profile shape in certain operational scenarios. At the same time, the decision-maker also settled for some ranks using all EOFs when the difference between top ranks appeared minimal.

There is no singular correlation when examining the relationship between the acoustic and environmental penalty for all CTDs. We can disregard the pattern from the first CTD due to insufficient depth information, though it raises important questions for through-the-sensor mechanisms. The second CTD shows an overall positive correlation, but there are two clusters; the second cluster shows a wide range of acoustic error with little variance in sound-speed error. These clusters are the dominant

features for the next four CTDs; the first cluster has a positive correlation and the second cluster has a negative one. The negative correlation here most likely stems from turning points in multiple surface-interacting rays realigning back to the original CTD pattern. The remaining XCTDs show weak positive correlations between the two penalties, with the exception of the one on March 11 1300, which uniquely has seemingly no correlation.

Overall, this shows the counterintuitive result that a minimal acoustic penalty can be driven by a varying range of environmental penalties. This information was rarely exploited by a human decision-maker for any individual CTD, as they were risk-averse in choosing an environmentally different but acoustically similar environment. The corollary, that minimal environmental penalties could produce a wide range of acoustic penalties, is technically true but is generally not possible because of how the EOFs reconstitute sound speed. These penalties are, of course, a function of the source depth and other parameters in the TDA configuration. Continued tactical simulations with the Virtual Ocean for vehicle operations will garner more data about this relationship.

V. SELECTED RESULTS

This section will explore three CTD casts to demonstrate the graphical TDAs, with a focus on the environmental and acoustic TDAs, respectively. The first case study uses the first

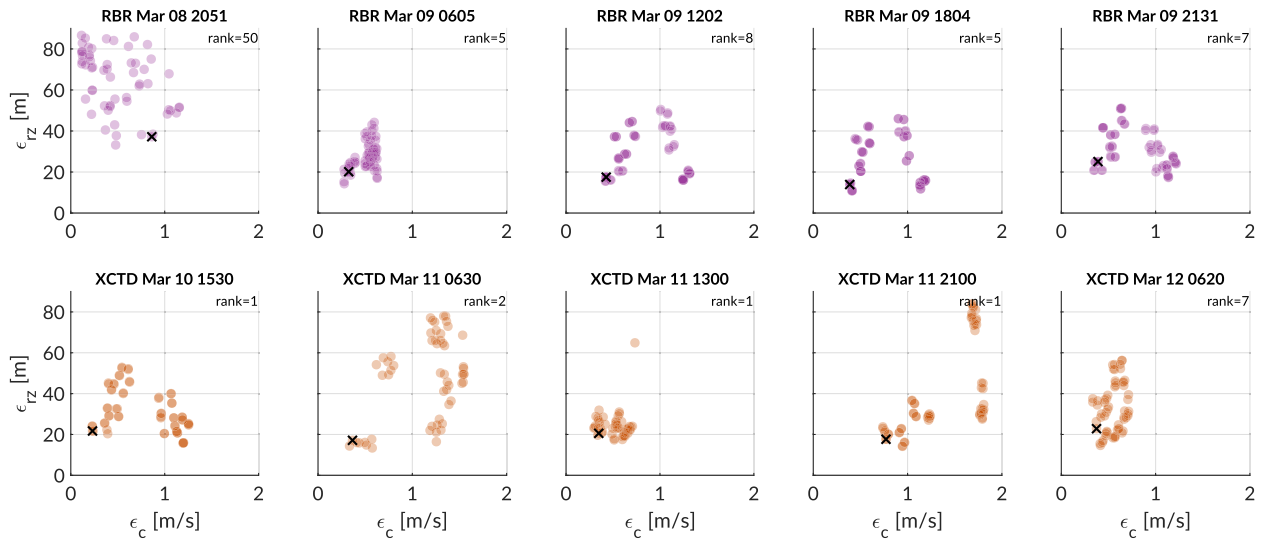


Fig. 9. Relationship between acoustic and environmental penalties for all ICEX20 CTDs. The x -axis shows the mean absolute error of the sound-speed ϵ_c and the y -axis shows the mean absolute error of the timefront eigenray shift, ϵ_{rz} . The black \times indicates the chosen sound-speed estimate’s penalties, where its rank is displayed in the top right corner.

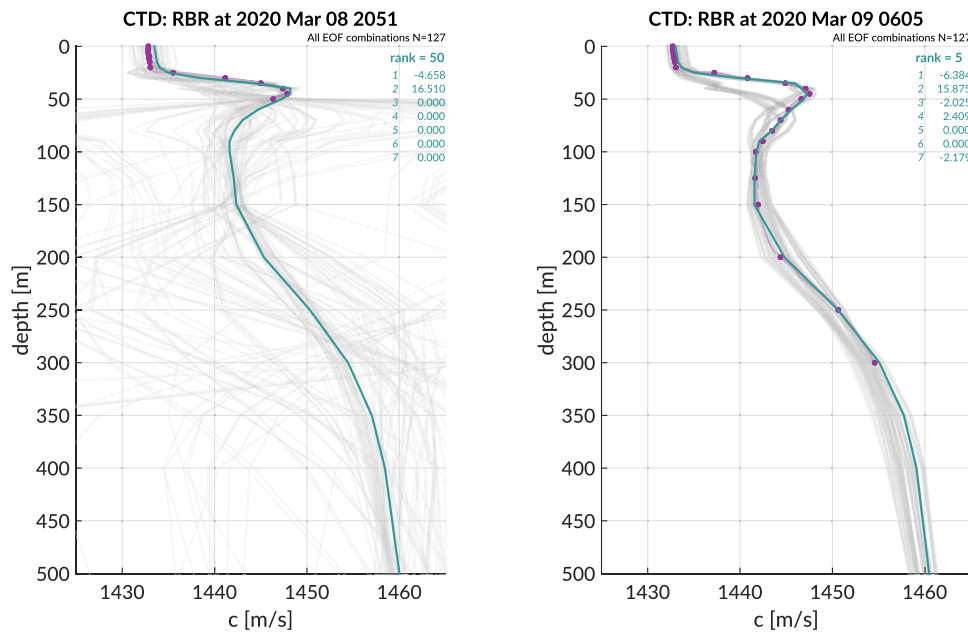


Fig. 10. Comparison of the first graphical TDA that shows all the combinations of sound-speed estimates (gray) compared to the desired sound speed (purple) and the chosen sound speed, rank, and weights (teal). On the left is the pipeline test CTD down to 50 m; on the right is the driving CTD that chose the EOF set.

two CTDs (RBR March 8 2051 and RBR March 9 0605); the second uses the seventh (XCTD March 11 0630). Code to demo the TDAs for any CTD cast is provided as a GitHub repository in Appendix VI.

A. Environmental TDAs

The first CTD taken on site tested the sensor functionality and the data pipeline; the cast only went down to 50 m. While

not used in the field, it, and the CTD cast 10 h later, provide an excellent window into sound-speed estimation beyond sensor depth, and the environmental TDAs.

Fig. 10 demonstrates the first TDA visualization of the sound-speed information. This TDA digests a user-entered sound speed and allows a user to match it to various EOF fits. The test CTD conjures several improbable sound-speed estimates because it overfits the minimal data available; the chosen rank is 50. The driving CTD for the mission, which was 10 h later,

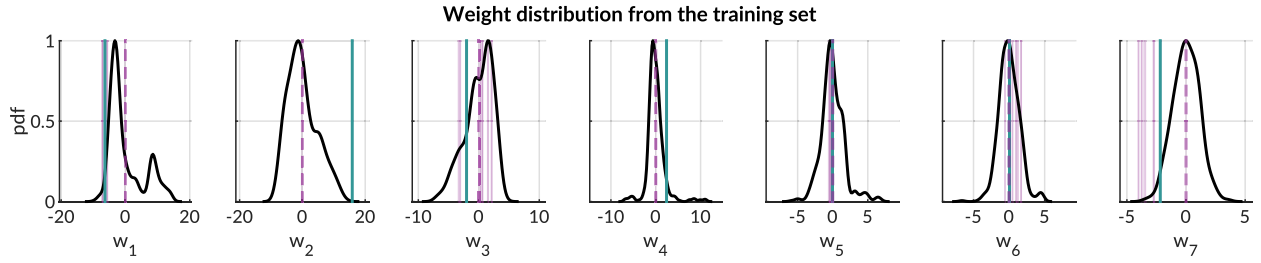


Fig. 11. This TDA shows *a priori* weight distribution from the EOF training set in black. Purple lines show the weights driving all sound-speed estimates and a teal line shows the weight for the chosen rank. The purple dashed line refers to weights that were manually tapped out as null.

corroborates the sound-speed estimate from the previous test CTD. The updated weights modify the first two from before and add the third, fourth, and seventh EOFs to the mix. This better reflects the data, especially between 50 and 100 m; and the TDA decision algorithm does a much better job suggesting this fit, with a rank of 5. The variation in sound speed fits at the surface encode different warming in the mixed layer; the variation from 50 to 100 m strangely encodes two different duct shapes (and strengths). At depths greater than 100 m, the window of the sound-speed estimates at any given depth is roughly 5 m/s.

The second environmental TDA, shown in Fig. 11, presents the discrete weights for all sound-speed estimates w versus the weight distribution from the training set β . Decision-makers were interested in sending the weights that most heavily and consistently deviated from the maximum likelihood. This is seen quite clearly for w_1 , w_2 , and w_7 , where the weights have little standard deviation and are located in a tail of the distribution. Less importance was attributed to a weight like w_3 , where the estimates spanned the full distribution (suggesting little impact), or w_5 , heavily centered at 0 (suggesting unnecessary forcing).

Overall, these two TDAs characterized the local Beaufort Lens and the error in the sound-speed estimation while contextualizing the estimate relative to the training distribution.

B. Acoustic TDAs

The second case study examines a weaker duct with the microlens around 45 m. This particular CTD is a compelling case study for the two acoustic TDAs because the chosen weights do not try to fit the microlens.

The first acoustic TDA visualizes the ray geometries between the ground truth SSP from the CTD and the estimated SSP from the VO. The user-entered time fronts are highlighted with increasing color to visualize the spread, but will be communicated with more granularity by the second acoustic TDA. The ray comparison by color and transparency is more intuitive than comparing color as an indicator for transmission loss differences, which has little bearing on navigation. In Fig. 12, one can see very little ray shift throughout the water column, even though the microlens is not considered. The multipath is well preserved; the rays that bound the shadow zone are slightly

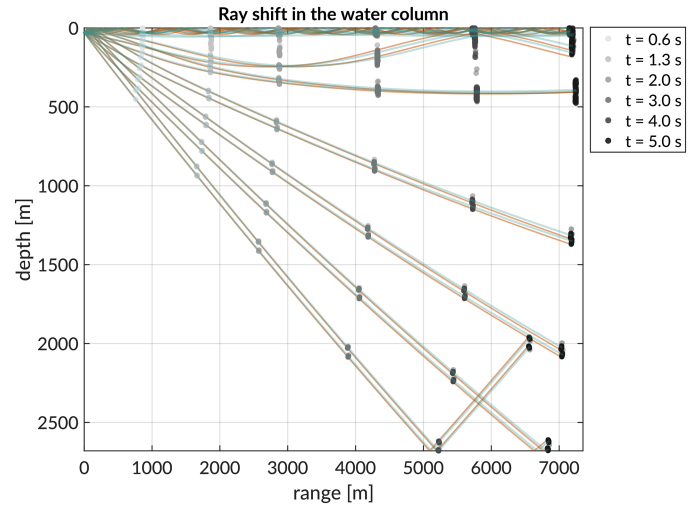


Fig. 12. This TDA displays the raytraces, or visual ray shift, for the CTD in orange and the EOF sound-speed estimate in teal. The legend indicates timefronts for all sound speed estimates, with color darkening with increasing travel time.

extended but not in any way to mislead position. The deeper rays are also preserved but were generally not considered to be of high importance because of our small operational domain. Thus, these ray geometries provide some insight as to what spatial scales of sound-speed features may impact downstream performance.

The second acoustic TDA delineates the relative ray shift over all launch angles by the suggested timefronts, as shown in Fig. 13. For rays represented by $\Gamma(\hat{c}, \theta)$, we define a unitless ray shift percentage

$$\text{range shift (\%)} = \frac{\epsilon_r}{P_r(c, t, \theta)} \times 100 \quad (11)$$

$$\text{depth shift (\%)} = \frac{\epsilon_z}{z_{\max}} \times 100 \quad (12)$$

where ϵ_r is the range component of ϵ_{rz} and $P_r(c, t, \theta)$ is the range component of P_{rz} . Effectively, range is normalized by the distance the ray has traveled and depth is normalized by the maximum water depth. The orange dot, referencing the desired ray position, centers the ray shift with no error. The numerous teal dots indicate the ray shift for all prescribed launch angles.

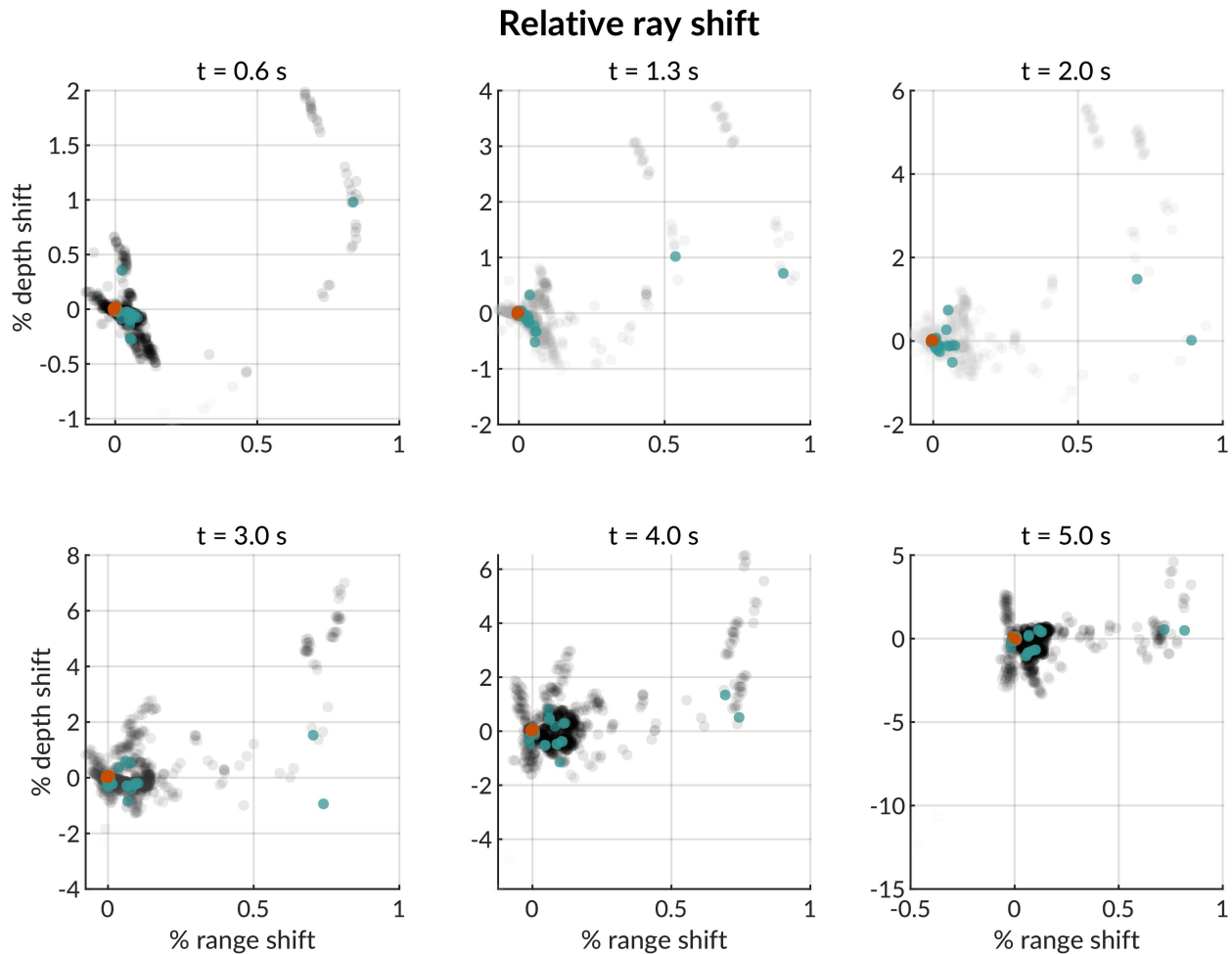


Fig. 13. This TDA displays the relative timefront eigenray shift as a percentage. The x-axis is the range error relative to the range traveled and the y-axis is the depth error relative to the water column depth. The gray dots show the relative ray shift for all sound-speed estimates and are darker for regions that have higher probability. The teal dots show the relative ray shift for the chosen sound-speed estimate for each launch angle. The orange dot is centered at $(0, 0)$, as this is the reference from the CTD.

The transparencies of the gray dots, referencing the ray shifts for all other sound-speed estimates, are weighted by the proximity to other ray shift estimates.

The relative ray shift allows for a strategic interpretation of range localization error sorted by pre-selected travel times. For example, if the user knows the vehicle is roughly a kilometer away and returning home, reducing the ray shift structure for 0.6 and 1.3 s may be more tactically important than the others. Alternatively, if the vehicle is at the same location and just starting its mission, the user may prioritize tightening the ray shift structure for larger travel times. Ultimately the second acoustic TDA provides a more granular approach to the relationship between mismatches in the sound-speed structure and their acoustic significance at times of interest. A byproduct of the relative ray shift, given the reliability of onboard pressure sensors, is a nominal estimate for the navigation error based on the acoustic propagation itself.

The major limitation for this interpretation is of course spatiotemporal variability in the water column. Given this is a fairly untenable problem for *in situ* observations or modeling, we

assume that an updatable range independent sound-speed profile is representative enough for small operational regions.

It should be noted that the observed range shift is almost always positive because the SSP estimate tends to be slightly greater than that of the SSP from the CTD. This is most obvious when the vehicle is near the surface and may even be true beyond the depth of the CTD. The time delay observed may be attributed to any ray's turning points in these overestimated regions. Ray shift plots for other CTDs show a more balanced negative and positive range shift.

VI. CONCLUSION

Based on our demonstration in the ice-covered Beaufort Sea, we conclude that this framework sufficiently addresses the need to consider the acoustic impact of a locally changing sound-speed profile in current underwater navigation paradigms. We have demonstrated that this tactical decision aid succinctly and effectively enables the use of an updatable, full water column profile rather than a single deterministic value for sound speed.

TABLE 1
AUTOMATICALLY PRESENTED RANKING BASED ON THE ENVIRONMENTAL AND ACOUSTIC PENALTIES

rank	EOF subset	sspError [m/s]	rayError [m]	raySTD [m]
1	1 2 4 6 7	0.418	15.51	18.89
2	1 2 4 5 6 7	0.423	15.60	18.84
3	1 2 4 5 7	0.478	16.09	21.19
4	1 2 4 7	0.471	16.13	21.47
5	1 2 3 4 7	0.427	17.49	24.64
6	1 2 3 4 5 7	0.427	17.50	24.62
7	1 2 3 4 6 7	0.427	17.49	24.65
8	1 2 3 4 5 6 7	0.427	17.50	24.63
9	1 2 5 6 7	0.564	20.20	20.60
10	1 2 6 7	0.559	20.69	22.09
11	1 2 7	0.598	20.44	21.75
12	1 2 5 7	0.604	20.65	22.77
13	1 2 3 5 7	0.559	26.34	26.04
14	1 2 3 5 6 7	0.564	26.47	26.24
15	1 2 3 7	0.557	26.75	26.57
16	1 2 3 6 7	0.562	26.85	26.76
17	2 4	1.247	15.98	11.98
18	2 4 5	1.247	16.05	12.47
19	1 2 4 5 6	0.624	28.69	25.75
20	1 2 4 6	0.623	28.76	25.90

From left to right: Rank is the z-score sorting of the metrics; EOF subset is which functions are used to generate the estimate; SspError is the mean absolute sound-speed error compared to the sound speed derived from the CTD; RayError is the Euclidean distance of specified eigenray timefronts between the CTD sound speed and the EOF estimate; raySTD is the standard deviation of the directional distance of the specified eigenray timefronts.

In doing so, our approach enables a human decision-maker to oversee an AUV in a way that promotes environmental awareness and trust in its autonomous capabilities. Future iterations of this framework could provide collaboration between submerged assets for enhanced spatiotemporal environmental awareness.

While EOF analysis is widely adopted for sound-speed reconstruction for its simplicity and effectiveness in capturing variability, it would behoove researchers to be cognizant of its acoustic implications. In this work, we smooth EOFs to encourage sound-speed continuity. One method to mitigate this manual smoothing, currently under investigation, is to include depth-dependent sound-speed gradients in the training feature space. To prioritize acoustic performance, we implement a real-time acoustic simulations and metrics in addition to the usual environmental fit in assessing weights. The lesson learned on this subject is that while a certain set of weights may produce a

sound-speed profile that is visually dissimilar to a desired one, the acoustic properties may be a closer match. To make this distinction clear to the human decision-maker, some pretraining on the impact of the acoustic parameters will be required before use. An improvement to this work would diversify the acoustic penalties into the communication realm without adding significant latency in the decision algorithm.

Given the Arctic's heightened sensitivity toward global climate change, we expect the spatio-temporal variability of the Beaufort Lens to continue to be a focus for oceanographers, acousticians, and roboticists alike. The approach presented here, which adapts to temporal changes in the sound speed, should be expanded to account for spatial variability—especially for long range applications. One can impose stochastic internal waves or encode 2-D probability distributions [69]. In addition, machine learning techniques like dictionary learning [70] may simplify weight finding and even reduce message size. In light of the

sound-speed profile estimation mismatch at 150 to 200 m in depth, there is a need to understand what depth grid resolution encodes variability optimally given the tradeoffs of limited source data and abundant microstructure.

It is also of extreme importance to maintain the quality of data garnered in the Canada Basin to continue to study the potential interactions between sea ice and the Beaufort Lens [67]. Because satellite ice cover data can be at daily resolution, linking the two may be a way to leverage the information disparity to further study warming of subsurface Arctic waters. More broadly speaking, the sea ice thickness dictates when these experiments can be done safely (generally only in March); but the Arctic's sensitivity to warming threatens these types of efforts and even invites a different ambient acoustic environment [71], [72].

This framework serves as a proof of concept for how we can leverage minimal acoustic communication to advance autonomy and is easily extendable to other underwater platforms and applications. For example, gliders would disproportionately benefit from not only the coupled environmentally adaptive communication and navigation paradigm but also from an updatable basis function representation to account for currents in the water column while path planning. Encoding other oceanographic parameters of interest, like temperature, salinity, or oxygen concentration, can create human-assisted feedback loops for more informed vehicle sampling to curate data sets of scientific value. This would be paradigm shifting for autonomous vehicle deployments where the data are of utmost scientific value and cannot easily be gathered any other way, such as a recent application where an AUV was constrained to fixed altitude paths to characterize warm water pathways underneath Thwaites Glacier [73].

As we seek to transition from teams of humans supervising a single vehicle toward teams of vehicles collaborating with little human supervision, a key focus of this work is building and maintaining operator trust in embedded AUV intelligence. TDAs are just one pathway to shift decision spaces into increasingly automated domains. Operations in the Beaufort Lens provided an excellent testbed to develop and demonstrate a type of information sharing that significantly improved autonomous navigation and communication behaviors. We hope this to continue this work to enable more intelligent multivehicle sampling, with geolocating oceanographic observations, to better understand the evolution and dynamics of oceanographically sensitive and acoustically complex environments.

APPENDIX

A1: GitHub Repository

A GitHub repository to demo the TDAs in this article for data taken during ICEx20 is available at <https://github.com/eeshanbot/ieee-bhatt-tda-demo/>.

A2: Table of Initial Ranking

See Table I.

ACKNOWLEDGMENT

The authors would like to thank the ICEx16 and ICEx20 field teams (S. Carper, R. Chen, D. Goodwin, T. Howe, A. Poulsen, T. Schneider, O. Viquez) who made this work possible; field efforts are always team efforts. The authors would also like to thank the Naval Postgraduate School for use of their CTD. The Ice-Tethered Profiler data were collected and made available by the Ice-Tethered Profiler Program (Toole *et al.*; Krishfield *et al.*) based at the Woods Hole Oceanographic Institution.¹ Lastly, the authors would like to thank IEEE Providence chapter for inviting E. Bhatt, R. Chen, and B. Howard to give a virtual talk about this work in October 2020.

REFERENCES

- [1] J. G. Bellingham and K. Rajan, "Robotics in remote and hostile environments," *Science*, vol. 318, no. 5853, pp. 1098–1102, Nov. 2007. [Online]. Available: <https://science.sciencemag.org/content/318/5853/1098>
- [2] Y. R. Petillot, G. Antonelli, G. Casalino, and F. Ferreira, "Underwater robots: From remotely operated vehicles to intervention-autonomous underwater vehicles," *IEEE Robot. Autom. Mag.*, vol. 26, no. 2, pp. 94–101, Jun. 2019.
- [3] J. Preisig, "Acoustic propagation considerations for underwater acoustic communications network development," *ACM SIGMOBILE Mobile Comput. Commun. Rev.*, vol. 11, no. 4, pp. 2–10, Oct. 2007. [Online]. Available: <https://doi.org/10.1145/1347364.1347370>
- [4] L. Paull, S. Saeedi, M. Seto, and H. Li, "AUV navigation and localization: A review," *IEEE J. Ocean. Eng.*, vol. 39, no. 1, pp. 131–149, Jan. 2014.
- [5] L. J. V. Van Uffelen, "Global positioning systems: Over land and under sea," *Acoust. Today*, vol. 17, no. 1, pp. 1–9, 2021.
- [6] S. Singh, M. Grund, B. Bingham, R. Eustice, H. Singh, and L. Freitag, "Underwater acoustic navigation with the WHOI micro-modem," in *Proc. IEEE OCEANS Conf.*, Boston, MA, USA, 2006, pp. 1–4. [Online]. Available: <https://ieeexplore.ieee.org/document/4099008/>
- [7] A. Gardner and J. Collins, "A second look at chip scale atomic clocks for long term precision timing," in *Proc. IEEE/MTS OCEANS Conf.*, Monterey, CA, USA, 2016, pp. 1–9.
- [8] R. M. Eustice, L. L. Whitcomb, H. Singh, and M. Grund, "Recent advances in synchronous-clock one-way-travel-time acoustic navigation," in *Proc. IEEE OCEANS Conf.*, 2006, pp. 1–6.
- [9] R. M. Eustice, L. L. Whitcomb, H. Singh, and M. Grund, "Experimental results in synchronous-clock one-way-travel-time acoustic navigation for autonomous underwater vehicles," in *Proc. IEEE Int. Conf. Robot. Autom.*, 2007, pp. 4257–4264.
- [10] S. E. Webster, R. M. Eustice, H. Singh, and L. L. Whitcomb, "Preliminary deep water results in single-beacon one-way-travel-time acoustic navigation for underwater vehicles," in *Proc. IEEE/RSJ Int. Conf. Intell. Robots Syst.*, 2009, pp. 2053–2060.
- [11] S. E. Webster, R. M. Eustice, H. Singh, and L. L. Whitcomb, "Advances in single-beacon one-way-travel-time acoustic navigation for underwater vehicles," *Int. J. Robot. Res.*, vol. 31, no. 8, pp. 935–950, Jul. 2012. [Online]. Available: <https://doi.org/10.1177/0278364912446166>
- [12] C. E. Graupe, L. J. van Uffelen, S. E. Webster, P. F. Worcester, and M. A. Dzieciuch, "Preliminary results for glider localization in the beaufort duct using broadband acoustic sources at long range," in *Proc. IEEE/MTS OCEANS Conf.*, Seattle, WA, USA, 2019, pp. 1–6.
- [13] S. E. Webster, L. E. Freitag, C. M. Lee, and J. I. Gobat, "Towards real-time under-ice acoustic navigation at mesoscale ranges," in *Proc. IEEE Int. Conf. Robot. Autom.*, 2015, pp. 537–544.
- [14] L. J. Van Uffelen, B. M. Howe, E.-M. Nosal, G. S. Carter, P. F. Worcester, and M. A. Dzieciuch, "Localization and subsurface position error estimation of gliders using broadband acoustic signals at long range," *IEEE J. Ocean. Eng.*, vol. 41, no. 3, pp. 501–508, Jul. 2016.
- [15] P. N. Mikhalevsky, B. J. Sperry, K. F. Wolfe, M. A. Dzieciuch, and P. F. Worcester, "Deep ocean long range underwater navigation," *J. Acoust. Soc. Amer.*, vol. 147, no. 4, pp. 2365–2382, Apr. 2020. [Online]. Available: <http://asa.scitation.org/doi/10.1121/10.0001081>
- [16] J. H. Kepper, B. C. Claus, and J. C. Kinsey, "MEMS IMU and one-way-travel-time navigation for autonomous underwater vehicles," in *Proc. IEEE OCEANS Conf.*, Aberdeen, U.K., 2017, pp. 1–9.

¹[Online]. Available: <https://www2.whoi.edu/site/itp/>

- [17] A. Litvak, "Acoustics of the deepwater part of the arctic ocean and of Russia's arctic shelf," *Herald Russian Acad. Sci.*, vol. 85, pp. 239–250, May 2015.
- [18] T. F. Duda, "Acoustic signal and noise changes in the beaufort sea pacific water duct under anticipated future acidification of arctic ocean waters," *J. Acoust. Soc. Amer.*, vol. 142, no. 4, pp. 1926–1933, Oct. 2017. [Online]. Available: <https://asa.scitation.org/doi/full/10.1121/1.5006184>
- [19] M. S. Ballard *et al.*, "Temporal and spatial dependence of a yearlong record of sound propagation from the Canada basin to the Chukchi shelf," *J. Acoust. Soc. Amer.*, vol. 148, no. 3, pp. 1663–1680, Sep. 2020. [Online]. Available: <http://asa.scitation.org/doi/10.1121/10.0001970>
- [20] A. J. Poulsen and H. Schmidt, "Acoustic noise properties in the rapidly changing arctic ocean," in *Proc. Meet. Acoust.*, vol. 28, 2016, Art. no. 070005. [Online]. Available: <http://asa.scitation.org/doi/abs/10.1121/2.0000552>
- [21] H. Schmidt and T. Schneider, "Acoustic communication and navigation in the New Arctic—A model case for environmental adaptation," in *Proc. IEEE 3rd Conf. Underwater Commun. Netw.*, 2016, pp. 1–4.
- [22] L. Freitag, K. Ball, J. Partan, P. Koski, and S. Singh, "Long range acoustic communications and navigation in the arctic," in *Proc. IEEE/MTS OCEANS Conf.*, Washington, DC, USA, 2015, pp. 1–5.
- [23] E. P. Chassignet *et al.*, "The HYCOM (HYbrid coordinate ocean model) data assimilative system," *J. Mar. Syst.*, vol. 65, no. 1, pp. 60–83, Mar. 2007. [Online]. Available: <https://www.sciencedirect.com/science/article/pii/S0924796306002855>
- [24] E. C. Bhatt, "A virtual ocean framework for environmentally adaptive, embedded acoustic navigation on autonomous underwater vehicles," Ph.D. dissertation, *Woods Hole Oceanograph. Institution Joint Program, Massachusetts Inst. Technol.*, Cambridge, MA, USA, Sep. 2021. [Online]. Available: <https://hdl.handle.net/1912/27309>
- [25] A. Adcroft, C. Hill, J.-M. Campin, J. Marshall, and P. Heimbach, "Overview of the formulation and numerics of the MIT GCM," in *Proc. ECMWF Seminar Ser. Numer. Methods, Recent Develop. Numer. Methods Atmos. Ocean Model.*, 2004, pp. 139–149.
- [26] T. F. Duda, W. G. Zhang, Y.-T. Lin, and A. E. Newhall, "Long-range sound propagation in the Canada Basin," in *Proc. 5th Underwater Acoust. Conf. Exhibit.*, 2019, pp. 483–490.
- [27] T. F. Duda, W. G. Zhang, and Y.-T. Lin, "Effects of pacific summer water layer variations and ice cover on beaufort sea underwater sound ducting," *J. Acoust. Soc. Amer.*, vol. 149, no. 4, pp. 2117–2136, 2021.
- [28] M. Kucukosmanoglu, J. A. Colosi, P. F. Worcester, M. A. Dzieciuch, and D. J. Torres, "Observations of sound-speed fluctuations in the beaufort sea from summer 2016 to summer 2017," *J. Acoust. Soc. Amer.*, vol. 149, no. 3, pp. 1536–1548, Mar. 2021. [Online]. Available: <https://asa.scitation.org/doi/full/10.1121/10.0003601>
- [29] S. Randeni, T. Schneider, and H. Schmidt, "Construction of a high-resolution under-ice AUV navigation framework using a multidisciplinary virtual environment," in *Proc. IEEE/OES Auton. Underwater Veh. Symp.*, 2020, pp. 1–7.
- [30] T. Schneider, H. Schmidt, and S. Randeni, "Self-adapting under-ice integrated communications and navigation network," in *Proc. 5th Underwater Commun. Netw. Conf.*, 2020, pp. 1–5.
- [31] S. Randeni, T. Schneider, H. Schmidt, E. Bhatt, and O. Viquez, "A high-resolution AUV navigation framework with integrated communication and tracking for under-ice deployments," *Field Robot.*, 2021, submitted for publication.
- [32] H. Björnsson and S. Venegas, "A manual for EOF and SVD analyses of climatic data," *CCGCR Rep.*, vol. 97, no. 1, pp. 112–134, 1997.
- [33] L. R. LeBlanc and F. H. Middleton, "An underwater acoustic sound velocity data model," *J. Acoust. Soc. Amer.*, vol. 67, no. 6, pp. 2055–2062, Jun. 1980. [Online]. Available: <https://asa.scitation.org/doi/10.1121/1.384448>
- [34] B. D. Cornuelle, "Inverse methods and results from the 1981 ocean acoustic tomography experiment," Ph.D. dissertation, Massachusetts Inst. Technol., Cambridge, MA, USA, 1983.
- [35] Y. Lin, A. E. Newhall, T. F. Duda, P. F. J. Lermusiaux, and P. J. Haley, "Merging multiple-partial-depth data time series using objective empirical orthogonal function fitting," *IEEE J. Ocean. Eng.*, vol. 35, no. 4, pp. 710–721, Oct. 2010.
- [36] J. K. Jensen, K. T. Hjelmervik, and P. Ostenstad, "Finding acoustically stable areas through empirical orthogonal function (EOF) classification," *IEEE J. Ocean. Eng.*, vol. 37, no. 1, pp. 103–111, Jan. 2012.
- [37] G. Casagrande, Y. Stephan, A. C. W. Varnas, and T. Folegot, "A novel empirical orthogonal function (EOF)-based methodology to study the internal wave effects on acoustic propagation," *IEEE J. Ocean. Eng.*, vol. 36, no. 4, pp. 745–759, Oct. 2011.
- [38] G. W. Pollitt, "Mine countermeasures (MCM) tactical decision aids (TDAs), a historical review," *Mil. Oper. Res.*, vol. 11, no. 3, pp. 7–17, 2006. [Online]. Available: <https://www.jstor.org/stable/43941044>
- [39] S. C. Collyer and G. S. Malecki, "Tactical decision making under stress: History and overview," in *Making Decisions under Stress: Implications for Individual and Team Training*. Washington, DC, USA: Amer. Psychol. Assoc., 1998, pp. 3–15.
- [40] D. H. Wagner, "Naval tactical decision aids," Defense Technical Information Center, Fort Belvoir, VA USA, Tech. Rep. ADA220401, Sep. 1989. [Online]. Available: <http://www.dtic.mil/docs/citations/ADA220401>
- [41] D. Duhon, "Tactical decision aid for unmanned vehicles in maritime missions," M.S. thesis, Naval Postgraduate School, Monterey, CA, USA, Mar. 2005. [Online]. Available: <https://apps.dtic.mil/sti/citations/ADA433030>
- [42] K. Wilson, "A prototype acoustic battlefield decision aid incorporating atmospheric effects and arbitrary sensor layouts," Army Res. Lab Adelphi, Adelphi, MD, USA, Tech. Rep. ADA353994, Sep. 1998. [Online]. Available: <https://apps.dtic.mil/sti/citations/ADA353994>
- [43] R. Grasso and S. Giannecchini, "Geo-spatial tactical decision aid systems: Fuzzy logic for supporting decision making," in *Proc. 9th Int. Conf. Inf. Fusion*, 2006, pp. 1–8.
- [44] N. Brown and C. Mueller, "Designing with data: Moving beyond the design space catalog," in *Proc. 37th Annu. Conf. Assoc. Comput. Aided Des. Architecture*, 2017, pp. 154–163.
- [45] A. Steinfeld *et al.*, "Common metrics for human-robot interaction," in *Proc. 1st ACM SIGCHI/SIGART Conf. Human-Robot Interact.*, 2006, pp. 33–40. [Online]. Available: <http://portal.acm.org/citation.cfm?doid=1121241.1121249>
- [46] M. Novitzky, P. Robinette, M. R. Benjamin, D. K. Gleason, C. Fitzgerald, and H. Schmidt, "Preliminary interactions of human-robot trust, cognitive load, and robot intelligence levels in a competitive game," in *Proc. IEEE/ACM Companion Int. Conf. Human-Robot Interact.*, Mar. 2018, pp. 203–204. [Online]. Available: <https://doi.org/10.1145/3173386.3177000>
- [47] M. Novitzky, H. R. R. Dougherty, and M. R. Benjamin, "A human-robot speech interface for an autonomous marine teammate," in *Proc. Int. Conf. Soc. Robot.*, 2016, pp. 513–520.
- [48] P. Norgren, R. Lubbad, and R. Skjetnet, "Unmanned underwater vehicles in arctic operations," in *Proc. 22nd IAHR Int. Symp. Ice.*, 2014, pp. 89–101.
- [49] L. D. Barker *et al.*, "Scientific challenges and present capabilities in underwater robotic vehicle design and navigation for oceanographic exploration under-ice," *Remote Sens.*, vol. 12, no. 16, pp. 1–31, 2020.
- [50] C. Kunz *et al.*, "Deep sea underwater robotic exploration in the ice-covered arctic ocean with AUVs," in *Proc. IEEE/RSJ Int. Conf. Intell. Robots Syst.*, 2008, pp. 3654–3660.
- [51] M. V. Jakuba *et al.*, "Long-baseline acoustic navigation for under-ice autonomous underwater vehicle operations," *J. Field Robot.*, vol. 25, no. 11/12, pp. 861–879, 2008. [Online]. Available: <https://onlinelibrary.wiley.com/doi/abs/10.1002/rob.20250>
- [52] A. Kukulya *et al.*, "Under-ice operations with a REMUS-100 AUV in the Arctic," in *Proc. IEEE/OES Auton. Underwater Veh.*, 2010, pp. 1–8.
- [53] A. Plueddemann, A. Kukulya, R. Stokey, and L. Freitag, "Autonomous underwater vehicle operations beneath coastal sea ice," *IEEE/ASME Trans. Mech.*, vol. 17, no. 1, pp. 54–64, Feb. 2012.
- [54] L. A. Stevens, F. Straneo, S. B. Das, A. J. Plueddemann, A. L. Kukulya, and M. Morlighem, "Linking glacially modified waters to catchment-scale subglacial discharge using autonomous underwater vehicle observations," *Cryosphere*, vol. 10, no. 1, pp. 417–432, 2016.
- [55] M.-L. Timmermans and P. Winsor, "Scales of horizontal density structure in the Chukchi sea surface layer," *Continental Shelf Res.*, vol. 52, pp. 39–45, 2013.
- [56] T. O. Fossum, P. Norgren, I. Fer, F. Nilsen, Z. C. Koenig, and M. Ludvigsen, "Adaptive sampling of surface fronts in the Arctic using an autonomous underwater vehicle," *IEEE J. Ocean. Eng.*, vol. 46, no. 4, pp. 1155–1164, Oct. 2021.
- [57] "Grid extract—download subsets of raster data," *Nat. Centers Environ. Inf.*, Boulder, CO, USA. Accessed: 2020. [Online]. Available: <https://maps.ngdc.noaa.gov/viewers/grid-extract/index.html>
- [58] F. B. Jensen, W. A. Kuperman, M. B. Porter, and H. Schmidt, *Computational Ocean Acoustics*. New York, NY, USA: Springer, 2011. [Online]. Available: <http://link.springer.com/10.1007/978-1-4419-8678-8>

- [59] M. B. Porter, "The BELLHOP manual and user's guide: Preliminary Draft," Heat, Light, Sound Res., Inc., La Jolla, CA, USA, Tech. Rep., 2011, vol. 260.
- [60] T. Schneider and H. Schmidt, "The dynamic compact control language: A compact marshalling scheme for acoustic communications," in *Proc. IEEE OCEANS Conf.*, Sydney, Australia, 2010, pp. 1–10. [Online]. Available: <https://ieeexplore.ieee.org/document/5603520/>
- [61] B. Howard, "Multi-path penalty metric in underwater acoustic communication for autonomy and human decision-making," Master's thesis, Woods Hole Oceanographic Institution Joint Program, Massachusetts Inst. Technol., Cambridge, MA, USA, 2021.
- [62] K. M. Thyng, C. A. Greene, R. D. Hetland, H. M. Zimmerle, and S. F. DiMarco, "True colors of oceanography: Guidelines for effective and accurate colormap selection," *Oceanography*, vol. 29, no. 3, pp. 9–13, 2016.
- [63] F. Fetterer, K. Knowles, W. Meier, M. Savoie, and A. Windnagel, "Sea ice index, Version 3," 2017. [Online]. Available: <https://nsidc.org/data/G02135/versions/3>
- [64] R. W. Helber, T. L. Townsend, C. N. Barron, J. M. Dastugue, and M. R. Carnes, "Validation test report for the improved synthetic ocean profile (ISOP) system, Part I: Synthetic profile methods and algorithm." Defense Technical Information Center, Fort Belvoir, VA, USA, Tech. Rep. ADA58521, Mar. 2013. [Online]. Available: <http://www.dtic.mil/docs/citations/ADA58521>
- [65] J. Toole, R. Krishfield, M.-L. Timmermans, and A. Proshutinsky, "The ice-tethered profiler: Argo of the arctic," *Oceanography*, vol. 24, no. 3, pp. 126–135, Sep. 2011. [Online]. Available: <https://tos.org/oceanography/article/the-ice-tethered-profiler-argo-of-the-arctic>
- [66] R. Krishfield, J. Toole, A. Proshutinsky, and M.-L. Timmermans, "Automated ice-tethered profilers for seawater observations under pack ice in all seasons," *J. Atmospheric Ocean. Technol.*, vol. 25, no. 11, pp. 2091–2105, Nov. 2008. [Online]. Available: <http://journals.ametsoc.org/doi/10.1175/2008JTECHO587.1>
- [67] J. A. MacKinnon *et al.*, "A warm jet in a cold ocean," *Nature Commun.*, vol. 12, no. 1, Apr. 2021, Art. no. 2418. [Online]. Available: <https://www.nature.com/articles/s41467-021-22505-5>
- [68] T. Schneider and H. Schmidt, "A state observation technique for highly compressed source coding of autonomous underwater vehicle position," *IEEE J. Ocean. Eng.*, vol. 38, no. 4, pp. 796–808, Oct. 2013. [Online]. Available: <https://ieeexplore.ieee.org/document/6572927/>
- [69] P. Krupskii, R. Huser, and M. G. Genton, "Factor copula models for replicated spatial data," *J. Amer. Statist. Assoc.*, vol. 113, no. 521, pp. 467–479, Jan. 2018. [Online]. Available: <https://doi.org/10.1080/01621459.2016.1261712>
- [70] M. Bianco and P. Gerstoft, "Dictionary learning of sound speed profiles," *J. Acoust. Soc. Amer.*, vol. 141, no. 3, pp. 1749–1758, Mar. 2017. [Online]. Available: <http://aip.scitation.org/doi/10.1121/1.4977926>
- [71] R. Chen, A. Poulsen, and H. Schmidt, "Spectral, spatial, and temporal characteristics of underwater ambient noise in the beaufort sea in 1994 and 2016," *J. Acoust. Soc. Amer.*, vol. 145, no. 2, pp. 605–614, Feb. 2019. [Online]. Available: <https://asa.scitation.org/doi/full/10.1121/1.5088601>
- [72] R. Chen and H. Schmidt, "Temporal and spatial characteristics of the beaufort sea ambient noise environment," *J. Acoust. Soc. Amer.*, vol. 148, no. 6, pp. 3928–3941, Dec. 2020. [Online]. Available: <https://asa.scitation.org/doi/full/10.1121/10.0002955>
- [73] A. K. Wählin *et al.*, "Pathways and modification of warm water flowing beneath Thwaites Ice Shelf, West Antarctica," *Sci. Adv.*, vol. 7, no. 15, Apr. 2021, Art. no. eabd7254. [Online]. Available: <https://advances.sciencemag.org/content/7/15/eabd7254>



EeShan C. Bhatt received the B.S.E. degree in mechanical engineering from Duke University, Durham, NC, USA, in 2015 and the Ph.D. degree in marine robotics and acoustical oceanography from Woods Hole Oceanographic Institution Joint Program, Massachusetts Institute of Technology, Cambridge, MA, USA, in 2021.

He is currently a Postdoctoral Investigator with the Woods Hole Oceanographic Institution. His research interests include embedded acoustic sensing and coordinated control across heterogeneous platforms for

ocean sampling.

Dr. Bhatt was the recipient of the NDSEG Fellowship in 2018.



Bradli Howard received the B.S. degree in nuclear engineering from North Carolina State University, Raleigh, NC, USA, in 2015 and the M.S. degree in acoustic communication metrics from the MIT-WHOI Joint Program, Massachusetts Institute of Technology, Cambridge, MA, USA, in 2021.

Before joining the MIT-WHOI Joint Program, she was stationed with the USS OHIO (BLUE) (SSGN 726) homeported with Bangor, WA, USA, and completed her tour as the Assistant Engineer and Operational Safety Officer. She is currently a Submarine

Officer. She earned her commission through the Naval Reserve Officer Training Corps (NROTC) Program.



Henrik Schmidt (Member, IEEE) received the M.S. and Ph.D. degrees from the Technical University of Denmark, Kgs. Lyngby, Denmark, in 1974 and 1978, respectively. He is currently a Professor of Mechanical and Ocean Engineering with the Massachusetts Institute of Technology, Cambridge, MA, USA. Before joining the MIT Faculty in 1987, he was a Senior Scientist with the NATO SACLANT ASW Research Centre, La Spezia, Italy. Early in his career, he developed numerically efficient numerical algorithms for the propagation of acoustic and seismic

waves in the ocean and solid earth environment, now used in more than 100 institutions around the world. In recent years, he has been pioneering in the development of new underwater acoustic sensing concepts for networks of small autonomous underwater vehicles for distributed MCM and ASW. He is the founder and Director of the MIT Laboratory for Autonomous Marine Sensing Systems, Cambridge, MA, USA (<http://lamss.mit.edu>). He was the Lead-PI and Chief Scientist for the multiinstitutional PLUSNet team developing a distributed, autonomous acoustic sensing concept, under the ONR Undersea Persistent Surveillance Program, in 2008 transitioned into the PLUS Program. He has been involved in several DARPA marine autonomy programs, including DASH, POSYDON, FAST, TEAC, and currently MantaRay. He has more than 80 refereed publications and coauthored a textbook on computational ocean acoustics. His research interests include underwater acoustic propagation and signal processing, and in recent years the development of integrated sensing, modeling, and autonomy for environmentally adaptive underwater acoustic sensing.

Prof. Schmidt is a Fellow of the Acoustical Society of America (ASA). He was the recipient of the ASA "Pioneer of Underwater Acoustics" medal in 2005.